2020-01-1075 Published 14 Apr 2020

An Integrated Model for Prediction of Process-Structure-Property Relationship for Additively Manufactured Al-10Si-Mg Alloy

Wenhua Yang, Zhuo Wang, Caleb Yenusah, and Yucheng Liu Mississippi State University

Citation: Yang, W., Wang, Z., Yenusah, C. and Liu, Y., "An Integrated Model for Prediction of Process-Structure-Property Relationship for Additively Manufactured Al-10Si-Mg Alloy," SAE Technical Paper 2020-01-1075, 2020, doi:10.4271/2020-01-1075.

Abstract

In this work, a process-structure-property relationship for additively manufactured Al-Si-Mg alloy was constructed, with the aid of an integrated multi-physics model. Specifically, first, a series of thermal simulations were performed to understand molten pool geometry under different additive manufacturing (AM) operating conditions, including laser beam power, scanning speed, and hatch spacing. The porosity formation was predicted based on thermal simulation results, which yield molten pool dimension information for predicting the lack-of-fusion porosity. Dream.3D was utilized to reconstruct synthetic microstructures with different volume fraction of porosity. Following that, with microporosity data as input, a widely employed Elasto-viscoplastic fast Fourier transformation (FFT) formulation was utilized to identify the structure-property-performance relationship, e.g. in the form of stress-strain curves, thus successfully constructed a full process-structure-property-performance (PSPP) map for the Al-Si-Mg alloy. Finally, by taking advantage of the PSPP map, the effective improvement of mechanical performance of AM product was analyzed through optimizing AM manufacturing conditions.

1. Introduction

Additive manufacturing (AM), including selective laser melting (SLM), selective laser sintering (SLS), directed energy deposition (DED), etc., is a process that joins materials to create a 3D component [1]. This manufacturing fashion brings about several advantages compared to the conventional subtractive manufacturing, in which the component of wanted geometry is, on the contrary, machined out of solid block of materials. Among them the major one is its great potential for fabricating component with complex geometry. A complicate component can be fabricated directly from the 3D computer aided design (CAD) model. Other advantages include the low waste and energy cost. For example, it adds material layer by layer so that usually what is required gets used. In this way, AM can reduce material costs and waste by as much as 90 percent. A good understanding of process-performance relationship through a process-structure-property-performance (PSPP) map can greatly help achieve product improvement through optimizing process conditions, thus enable us to make better use of the AM technology. Specifically, using selective laser beam melting (SLBM) (one type of powder-bed fusion AM) of Al-10Si-Mg alloy as an example, in this project we will utilize an integrated multi-scale multi-physics model to build up a PSPP map for process optimization.

To construct the PSPP map, the first step is to find out the process-structure relationship. In this study, the structure of our interest is the grain microstructure and microporosity developed under different process conditions of laser beam power, scanning speed and hatch spacing. As we know, the grain microstructure can greatly affect the final product performance. For instance, due to the existence of steep thermal gradient in and around the molten pool in AM process, large columnar grains by directional epitaxial growth tend to be formed, resulting in large mechanical anisotropy of as-built component. It has been pointed out; the coarse columnar grain structure can cause premature failure in the transverse loading. In addition, as temperature and liquid volume fraction decrease, volumetric solidification shrinkage and thermal contraction in these channels produces cavities and hot tearing cracks which may span the entire length of the columnar grain and can propagate through additional intergranular regions. In contrast, fine equiaxed microstructures more easily accommodate strain in the semi-solid state by suppressing coherency that locks the orientation of these solid dendrites and promotes tearing [2]. Microporosity also plays a critical role in determining the mechanical performance of final AM product [3]. There are mainly two types of porosity formed during metal-based AM process, namely keyhole and lack-of-fusion pore. The former is formed due to keyhole-model laser/EB heating under certain conditions. In this case, strong evaporation of the metal occurs and results in very deep pool. The collapse of the deep cavity finally gives birth to the keyhole pores [4].

In current study, we mainly focus on the more common lack-of-fusion pores. This type of pore basically stems from the insufficient overlap of successive melt pools. A good example is the interlayer porosity, which are formed due to small pools from the new layer that propagate down to barely contact the surface of the previous layers. There are also inter-track pores that are

developed by a similar mechanism. The lack-of-fusion thus highly depends on the pool dimensions under various manufacturing parameters including laser power, scanning speed, hatching space and powder layer thickness. Thus, plenty of work has been devoted to predicting the porosity level. In this work, a well approved analytical model [5] was adopted to predict porosity caused by insufficient overlap of melt pools lack of fusion. Specifically, in the calculation of porosity volume fraction, melt-pool cross-sectional dimensions, hatch spacing, and layer thickness were considered. This approach has showed fast prediction of the effects of changes in processing parameters on the porosity of the AM metal parts using simple Rosenthal equation. In our study, an well validated finite element method [6, 7, 8] was utilized instead to simulate the molten pool dimensions under different process parameters during AM. Dream.3D was employed to synthesize the polycrystalline with different microporosity. Since in this study, porosity effect on mechanical property of AM is our focus, grain morphology was constructed as equiaxed, while irregular pore shape was considered according to reported experiment images of the AM metal parts.

The second step is to build up the structure-property-performance relationship to complete the full PSPP map. Numerous numerical studies have been performed to understand the structure-property relation for metallic AM fabrication. Yan et al. [9, 10] have explored the effect of powder bed on the heat transfer, melt pool dimension and porosity of building parts using an integrated discrete element method and computational fluid dynamics (CFD) method. They concluded, to a large extent, that the input energy and powder layer thickness determined the quality of as-built products during metallic powder bed-based AM. However, their computational framework failed to predict the micromechanical fields due to the influence of local variations in the microstructure. In recent years, Lebensohn has extended the fast Fourier transform (FFT)-based formulation for predicting the deformation of polycrystals in the elasto-viscoplastic regime (EVP). The EVP-FFT formulation has been well validated to predict the local micromechanical fields and effective mechanical behavior of heterogeneous materials [11, 12].

Thus, in this work, an integrated multi-scale multi-physics model is presented here as depicted in Figure 1. The proposed framework provides systematical insights into the process-microstructure-property relationship during AM of Al-Si-Mg alloy. The porosity formation was predicted based on thermal simulation results of an finite element method (FEM) model, which yield molten pool dimension information for predicting the lack-of-fusion porosity. Dream.3D was utilized to reconstruct synthetic microstructures with different volume fraction of porosity. The computationally efficient EVP-FFT model was employed to fully investigate the crystal plasticity and accurately predict the micromechanical behavior.

FIGURE 1 Schematic representation of the integrated multi-scale multi-physics model illustrating the novel computational framework for investigating process-microstructure-property relationship optimization cycle.

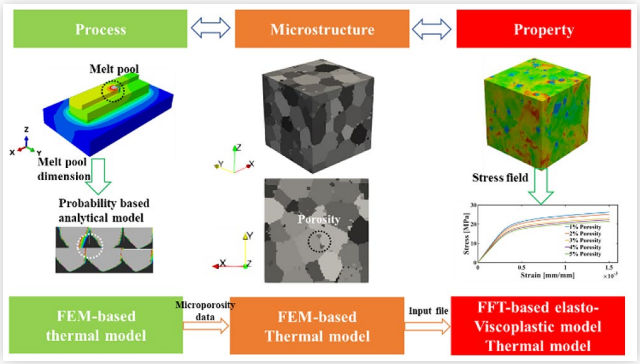

2. Model

It is widely known that the mechanical property of as-fabricated AM product is largely determined by its microstructure including grain structure and microporosity. In our study, we used a combined model (Dream. 3D, internal state variable (ISV) model and EVPFFT) to study the microstructure formation under different processing conditions, as well as predict corresponding property and performance. This enabled us to construct the PSPP map, which would provide guidelines in enhancing the performance of additively manufactured products by optimizing their fabrication conditions. Specifically, predictions of both grain structure and porosity development are based on finite element based AM thermal simulations. That is the microporosity development dictated by the pool geometry that relies on the thermal simulation. Finally, with the grain structure and microporosity as input, the ISV model and EVPFFT were utilized to predict the corresponding performance, e.g. the stress-strain curve.

2.1. Model for Predicting Process-Structure Relationship

2.1.1. Finite Element Based Thermal Model A multilayer and multitrack thermal model as depicted in Figure.1 on the basis of element birth and death technique was first used to predict temperature field development under different AM processing conditions. The simulation starts with multiple layers of activated substrate elements, and then new layers of element are sequentially (at a time interval of t) activated to essentially mimic the layer-by-layer deposition of materials in practice. The thermal model is mainly based on the classical heat transfer equation:

$$\nabla\cdot\left(k\nabla T\right)+\rho Q_e=\frac{\partial\left(\rho h\left(T\right)\right)}{\partial t} \qquad \text{Eq. (1)}$$

where T(r, t) is a tempo-spatial temperature field, and Q_e denotes the body heat density. h(T) is the enthalpy per unit mass, which incorporates the latent heat of the phase change. The material parameters of Al-Si-Mg alloy in Equation (1) include thermal conductivity k, density ρ, and specific heat c_p.

The heat dissipation is contributed by both the convective and radiative heat transfer at the surface, which is described as:

$$k\nabla \cdot T = h\left(T_a - T\right) + \varepsilon_R \sigma_R \left(T_a^4 - T^4\right) \quad \text{Eq. (2)}$$

where T_a is the ambient temperature, h is the heat convection coefficient, ε_R, σ_R are emissivity and Stefan-Boltzmann constant (5.67 × 10-8 W/m2·K4), respectively.

When a porous material interacts with the laser, the laser penetration depth (η) of the powder layer should be considered. In this model, the laser penetration depth of the AlSi10Mg powder was regarded as one thickness of powder layer [13]. The Gaussian heat source was represented as:

$$q(x,y,z,t) = \frac{2\alpha G}{\pi r^2 \eta} \cdot \exp\left[-2\frac{x^2+y^2}{r^2}\right] \exp\left(-\frac{|z|}{\eta}\right) \quad \text{Eq. (3)}$$

where G is the laser power, r is the laser beam radius corresponding to the distance between the beam center and the point. α is the laser energy absorptivity (0.60) of a material, which is affected by the wavelength of the laser and can be measured by a diffuse reflectance spectroscopy. η is the laser penetration depth of the AlSi10Mg powder. The laser energy density reduced to both horizontal direction and depth direction at the center of the laser spot [14].

The governing equations (1-4) are solved on an ABAQUS 2017 platform.

2.1.2. Synthetic Microstructure Generation Via Dream.3D

DREAM.3D developed by Groeber and Jackson has been extensively used to generate microstructure-based models for simulations. It can be used as a platform for developing the processing 3D orientation map. The 3D orientation map can be built on a regular grid that can be used as an input into simulations using the FFT method to determine the mechanical response of materials subjecting to mechanical loads. In addition, it can be used to create meshed models of microstructures that can then be exported in formats that are accepted by standard finite element analysis (FEA) software packages.

In this study the former approach was adopted for the synthetic microstructure generation of the additively manufactured Al10SiMg. Specifically, different pipelines were employed to define the desired polycrystals with different volume fractions of porosity as depicted in Figure 2. The defined polycrystals were then exported as Los Alamos FFT files. In particular, the pore shape was irregular in accordance with reported images in published literature as shown in Figure 3. These microstructures had equiaxed grains with normal size distribution and was discretized using a regular grid, $\{x^d\}$, whose size is 128 × 128 × 128. All grids used in EVPFFT have the same size.

FIGURE 2 Schematic representation of the solution domain, including substrate, powder bed. x, y, z represents the scanning, hatching, and building directions, respectively.

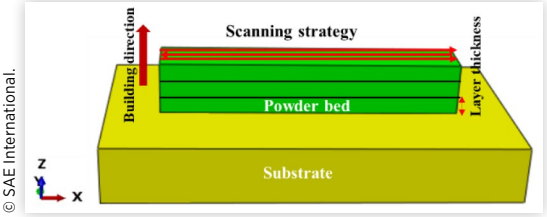

FIGURE 3 The comparison of morphology between experimental model [12] (a) and numerical model (b).

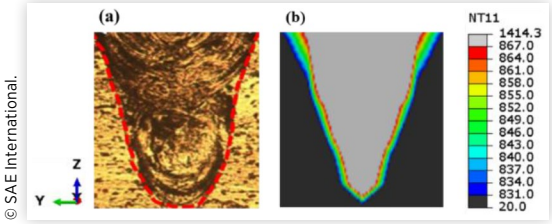

2.2. Elasto-Viscoplastic FFT Formulation

This work employed an extended FFT-based formulation in the elasto-viscoplastic regime [15] for the prediction of the local micromechanical fields and effective mechanical behavior of the AM manufactured porous Al-Si-Mg alloy under different process parameters. Although, the original rigid-viscoplastic (VP) regime can be used to study both macroscopic and microscopic aspects of polycrystal deformation, for problems, in which the elastic and plastic strains are comparable in magnitude and/or when the full stress tensor field needs to be determined, the EVP-FFT regime that encompasses both regimes has the ability of to simultaneously account for elastic and viscoplastic effects in porous polycrystals is more appropriate in our study.

The FFT-based formulation provides an exact solution for periodic unit cells of the governing equations of stress equilibrium and strain compatibility. Equilibrated stress and compatible strain fields are adjusted iteratively to simultaneously satisfy the required constitutive relation. Fourier transform of Green functions of a periodic linear reference medium and convolution integrals, evaluated efficiently in Fourier space, are used to solve the micromechanical problem.

Since the details can be referred to [15], here we only present the basics of the elasto-viscoplastic FFT formulation for polycrystals. The viscoplastic part of the strain-rate $\dot{\varepsilon}^p(x)$ is constitutively related to the stress $\sigma(x)$ at a single-crystal material point x through a sum over the N active slip systems, with the form:

$$\dot{\boldsymbol{\varepsilon}}^{\mathrm{p}}(\mathbf{x}) = \sum_{s=1}^{N} \mathbf{m}^{s}(\mathbf{x})\dot{\gamma}^{s}(\mathbf{x}) = \dot{\gamma}_o \sum_{s=1}^{N} \mathbf{m}^{s}(\mathbf{x}) \left(\frac{\left|\mathbf{m}^{s}(\mathbf{x}) : \boldsymbol{\sigma}(\mathbf{x})\right|}{\tau_o^s(\mathbf{x})} \right)^n \times \mathrm{sgn}\left(\mathbf{m}^{s}(\mathbf{x}) : \boldsymbol{\sigma}(\mathbf{x})\right) \quad \text{Eq. (4)}$$

where $\dot{\boldsymbol{\gamma}}^{s}(\mathbf{x})$, $\tau_o^s(\mathbf{x})$ and $\mathbf{m}^{s}(\mathbf{x})$ are, respectively, the shear rate, the critical resolved shear stress (CRSS) and the (symmetric) Schmid tensor, associated with slip system(s) at point $\mathbf{x}$; $\dot{\gamma}_o(\mathbf{x})$ is a normalization factor, and n is the rate-sensitivity exponent. Owing to strain hardening, the CRSS of the slip system(s) is,

in general, a function of accumulated plastic strain in the crystal, in turn a function of the stress.

A Euler implicit time discretization combined with Hooke's law with the assumption of small strains is employed to solve the elasto-viscoplastic problem. The stress and strain in material point x at t are written as:

$$\boldsymbol{\sigma}(\mathbf{x}) = \mathbf{C}(\mathbf{x}) : \left(\boldsymbol{\varepsilon}(\mathbf{x}) - \boldsymbol{\varepsilon}^{p,t}(\mathbf{x}) - \dot{\boldsymbol{\varepsilon}}^{p}(\mathbf{x},\boldsymbol{\sigma})\Delta t\right) \quad \text{Eq. (5)}$$

$$\boldsymbol{\varepsilon}(\mathbf{x}) = \mathbf{C}(\mathbf{x}) : \boldsymbol{\sigma}(\mathbf{x}) + \boldsymbol{\varepsilon}^{p,t}(\mathbf{x}) + \dot{\boldsymbol{\varepsilon}}^{p}(\mathbf{x},\boldsymbol{\sigma})\Delta t \quad \text{Eq. (6)}$$

where $\sigma(\mathbf{x})$ is the Cauchy stress tensor, $C(\mathbf{x})$ is elastic stiffness tensor, $\varepsilon(\mathbf{x})$, $\varepsilon^{e}(\mathbf{x})$ and $\varepsilon^{p}(\mathbf{x})$ are the total, elastic and plastic strain tensors, and $\dot{\varepsilon}^{p}(\mathbf{x})$ is the plastic strain-rate tensor given by Equation (4).

Adding and subtracting the team $C^{o}_{ijkl}u_{k,l}(\mathbf{x})$ to or from the stress tensor of Equation (5), where C^{o}_{ijkl} is the stiffness of reference medium and $u_{k,l}(\mathbf{x})$ is the displacement-gradient tensor, gives:

$$\sigma_{ij}(\mathbf{x}) = C^{o}_{ijkl}(\mathbf{x})u_{k,l}(\mathbf{x}) + \varphi_{kl}(\mathbf{x}) \quad \text{Eq. (7)}$$

where the polarization field is given by:

$$\varphi_{ij}(\mathbf{x}) = \sigma_{ij}(\mathbf{x}) - C^{o}_{ijkl}u_{k,l}(\mathbf{x}) = \sigma_{i,j}(\mathbf{x}) - C^{o}_{ijkl}\varepsilon_{kl}(\mathbf{x}) \quad \text{Eq. (8)}$$

Combining Equation (7) with the equilibrium condition $\sigma_{ij,j}(\mathbf{x}) = 0$ we can have:

$$\varphi_{ij}(\mathbf{x}) + C^{o}_{ijkl}u_{k,l}(\mathbf{x}) = 0 \quad \text{Eq. (9)}$$

Equation (9) can be solved for a periodic unit cell under an applied strain $\mathbf{E} = (\boldsymbol{\varepsilon}(\mathbf{x}))$ using the Green function method, i.e.

$$C^{o}_{ijkl}G_{km,lj}(\mathbf{x} - \mathbf{x}') + \delta_{im}\delta(\mathbf{x} - \mathbf{x}') = 0 \quad \text{Eq. (10)}$$

where $G_{km}(\mathbf{x})$ is the Green function associated with the displacement field $u_k(\mathbf{x})$. The displacement gradient is given by a convolution integral:

$$u_{k,l}(\mathbf{x}) = \int_{R^3} G_{ki,jl}(\mathbf{x} - \mathbf{x}')\varphi_{IJ}(\mathbf{x}')d\mathbf{x}' \quad \text{Eq. (11)}$$

which can be solved in the Fourier space using the convolution theorem, the compatible strain field derived from the solution of Equation (9) is given by.

$$\varepsilon_{ij}(\mathbf{x}) = E_{ij} + FT^{-1}\left(sym\left(\hat{\Gamma}^{0}_{ijkl}(\mathbf{k})\right)\hat{\varphi}_{kl}(\mathbf{k})\right) \quad \text{Eq. (12)}$$

where the symbol "^" indicates the Fourier transform and k is a point (frequency) of the Fourier space.

The FFT-based method consists evaluating the above expressions in points and frequencies belonging to regular grids (of the same size) in the Cartesian and Fourier spaces, respectively, in which case, the direct and inverse Fourier transforms in Equation (12) become discrete, and the FFT algorithm can be applied.

Equation (12) is a fix-point equation for the strain field that allows for solving the constative and governing equations iteratively. In practice, for a better convergence of our micro-mechanical model for the AM microstructures, a modified version of the above algorithm was adopted, based on the augmented Lagrangian formulation presented by Michel and Moulinec [16], and adapted to the EVP polycrystals.

In the current model, an extended Voce law is used and defined as the form:

$$\tau^{n}(\Upsilon) = \left(\tau^{*}_{0}\right)^{n} + \left(\tau^{n}_{1} + \theta^{n}_{1}\right)\left(1 - \exp\left(-\Upsilon\left|\frac{\theta^{n}_{0}}{\tau^{n}_{1}}\right|\right)\right) \quad \text{Eq. (13)}$$

The total accumulated shear strain $\Upsilon(\mathbf{x}) = \sum_{t=1}^{N_t}\sum_{n=1}^{N}\dot{\gamma}^{n}(\mathbf{x},t)\Delta t$,

where N_t is the number of time increment and N is total number of slip system. θ_0 and θ_1 are the initial and asymptotic hardening rates, respectively, $(\tau_0 + \tau_1)$ refers to the back-extrapolated stress, τ^{*}_{0} is initial yield stress.

3. Result and Discussion

3.1. Process-Structure Relationship

Figure 2. depicts the computational domain that consists of powder bed, substrate and 3 layers-3 hatches build. The x, y and z directions represent the scanning, hatching, and building directions, respectively. A reciprocating scanning strategy was adopted, i.e. laser beam travels in positive x direction in the first hatch and return in negative x direction in the second hatch, and so forth. Table 2 lists the process parameters and dimensions of the computational domain used in the calculations. The properties of the AlSi10Mg powder is provided in Table 1 [17].

3.1.1. Temperature Field

Figure 3 depicts the experimental and numerical cross-section morphologies of the molten pool under the laser power 400 W and scanning speed 0.3 m/s. The region within the bold red colored line indicates isotherm curves of numerical simulation, where the temperature exceeded the liquidus temperature (867 K). The region bounded by the red and green lines is the mushing zone, where the temperature is between the liquidus and the solidus temperature of AlSi10Mg. As illustrated in that figure, the shape of fusion zone is quite identical between the experimental and numerical results.

TABLE 1 Process parameters adopted to perform AM simulations.

Parameters	Value
Laser power, (W)	250, 300, 350, 400, 450, 550, 600, 650
Scanning speed, (m/s)	0.1, 0.2, 0.3, 0.4, 1, 2, 3
Spot radius, (mm)	0.2
Layer thickness, (mm)	0.3
Hatch spacing, (mm)	0.3, 0.45
Building length, (mm)	5.28
Substrate dimensions, (mm × mm × mm)	7.71 × 4 × 1

TABLE 2 Thermo-physical properties of AlSi10Mg. Here "T" represents temperature in K and ranges from ambient to the solidus temperature.

Properties	AlSi10Mg
Liquidus temperature (K)	867
Solidus temperature (K)	831
Thermal conductivity (W/m K)	113 + 1.06 × 10^{-5} T
Specific heat (J/Kg K)	536.2 + 0.035 T
Density (kg/m^3)	2670
Latent heat of fusion (J/Kg)	423 × 10^3
Absorption coefficient	0.6
Young's modulus	68

Figure 4 illustrates the computed transient temperature fields with different laser powers at the same laser beam scanning speed (0.3 m/s) during the first layer and first hatch build. The molten pools are elongated in negative x direction because the laser beam travels in the positive direction. The molten pools exhibit a tear drop shape due to a relatively fast scanning speed used in the calculation. As can be noticed, the maximum temperature increased with the increase of laser powers, resulting in increased molten pool dimensions (Figure 6), which can be simply explained by the intense heat input with larger laser power. Figure 6 shows the depths of all the molten pools are larger than the layer thickness (0.3 mm), which would be beneficial to assure the interlayer bonding. On the other hand, the molten pool widths of the selected process parameters as depicted in Figure 6 (a) and (b) is 480 and 563 µm, respectively. They are not wide enough and would probably induce inter-hatch type of lack of fusion depending on the magnitude of hatch spacing, which will be further explained in the next section.

Figure 5 shows the temperature distribution under different scanning speeds at a fixed laser power 400 W during the first layer first hatch build. On contrary to the laser power

FIGURE 4 Temperature fields and molten pools developed under different laser beam powers at the same laser scanning speed 0.3 m/s during the first layer first hatch build of 0.45 mm hatch spacing. From (a)-(d), respectively, 450 W, 500 W, 550 W, and 600 W. Scanning direction of laser beam is along the positive x direction.

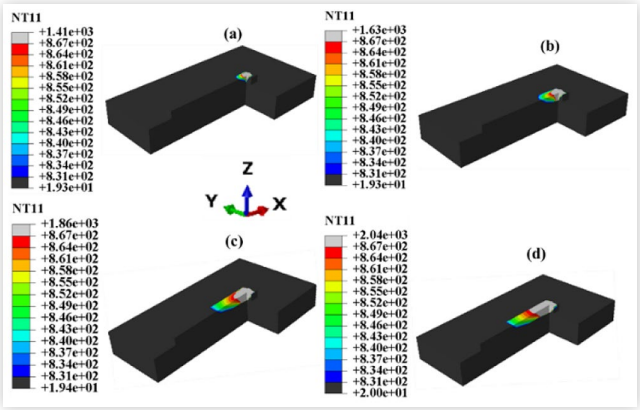

FIGURE 5 Temperature fields and molten pools developed under different laser scan speeds at the same laser power 400 W during the first layer first hatch build of 0.6 mm hatch spacing. From (a)-(d), respectively, 0.1 mps, 0.2 mps, 0.3 mps, and 0.4 mps. Scanning direction of laser beam is along the positive x direction.

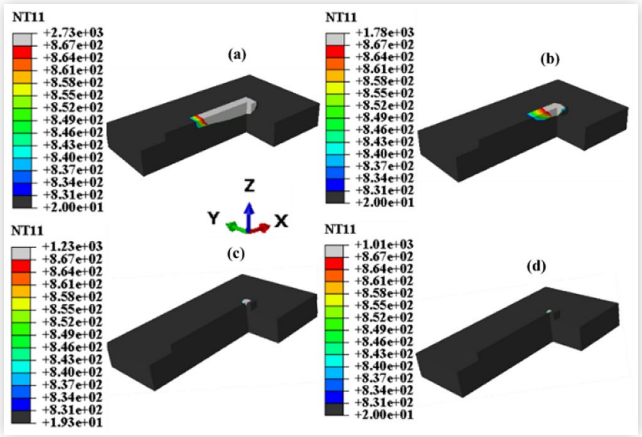

FIGURE 6 y-z Cross section view of a molten pool under different laser beam powers at the same laser scanning speed 0.3 m/s during the first layer and second hatch build of 0.45 mm hatch spacing. From (a)-(d), respectively, 450 W, 500 W, 550 W, and 600 W. Scanning direction of laser beam is along the positive x direction.

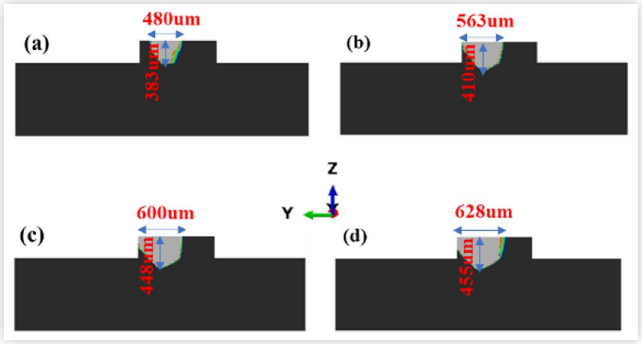

effect, increased scanning speed would induce a lower peak temperature caused by a reduced net amount of heat input per unit length (laser × velocity). Thus, a higher scanning speed may increase the production efficiency, but has high risk of formation of lack of fusion with the decreased molten dimensions. Figure 7 illustrates the effects of laser beam power and scanning speed on the molten pool dimensions. As can be noticed, an increased laser power and/or a reduced scanning speed would increase the dimensions of the fusion zone. The ratio of length and width/depth increase with a higher laser power and/or lower scanning speed. The phenomenon may be attributed to the fact that the increased laser energy absorption provides sufficient volume of melt and accordingly a relatively large solidification zone with higher thermal conductivity as the laser beam moves away [18].

FIGURE 7 Molten pool dimensions during the first layer and first hatch build with (a) different laser powers (scanning speed 0.3 m/s), and (b) different laser beam scanning speeds (laser beam power 400 W).

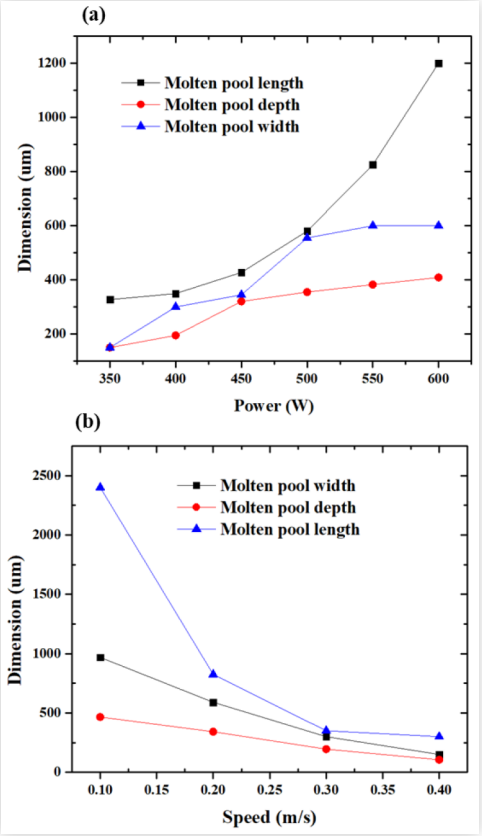

3.1.2. Lack of Fusion Porosity Calculation

The calculation approach adopted in this study indicates that the depth of overlap (L*; see Figure 8) between laterally adjacent melt pools plays a significant role in determining complete melting [4]. It stated that the layer thickness L should be less than the overlap L* would induce lack of fusion porosity.

This calculation approach has two options, one is implemented in Python, the other is calculated in spreadsheet. But it stated that these two simulations provided the same estimates of the unmelted volume fractions with the same input values. For simplicity, the faster simulation was employed in this study and summarized, more details can be referred to [4].

FIGURE 8 Schematic of the assumed dual half-ellipse shape of melt pools with relevant dimensions labeled, showing the overlap between two adjacent beads.

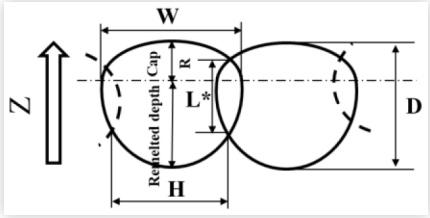

Basically, calculating the probability that positions in a plane at a certain vertical position would not be melted during the deposition of any of the layers would provide estimates of the porosity. As illustrated in Figure 9 the δ_{01}/H gives the probability that positions at the top of layer 1would remain unmelted after the first pass. δ_{01} is the shortest distance between the melt pools at the top of this layer. This position would have a probability δ_{02}/H not being melted during the deposition of the next layer, and of δ_{03}/H when the third layer was deposited. Thus, the overall probability of this position remaining unmelted after three passes would be given by $(\delta_{01}/H \times \delta_{02}/H \times \delta_{03}/H)$. Likewise, $(\delta_{L1}/H \times \delta_{L2}/H)$ would be the probability of remaining unmelted for the positions one-layer thickness (L) below the top of layer 1 because layer 3 shown in this example did not extend down to this level. At least 100 positions distributed vertically over the distance L from the top of layer 1 was required to perform this calculation. A numerical integration was performed to find the overall probability of positions in one layer remaining unmelted. The distance can be found readily according to the geometry of the dual half-elliptical melt pools. After the fraction of the unmelted volume ε in the part was obtained, the density of the part relative to a fully dense material was given by the following equation.

$$\frac{\rho_{part}}{\rho_{true}} = 0.64\varepsilon + 0.991(1-\varepsilon) \qquad \text{Eq. (14)}$$

Figure 9 presents a case where the layer thickness is between one-half and one-third the melt-pool depth. For the molten pool geometry in this study, the calculation approach is still applicable [4].

Insufficient fusional bonding between hatches and layers causes the lack of fusion defects [19]. Thus, these defects significantly depend on the molten pool dimensions, laser power, scanning speed, layer thickness and hatch spacing. Figure 10 depicts the influence of these process parameters on the lack of fusion voids. The porosity values were obtained by the calculation approach mentioned above with the width, depth of fusion zone, hatch spacing and layer thickness (fixed as 0.3 mm) as inputs, which were computed from the FEM thermal model. As can be noticed from that figure, a higher hatching spacing would induce a larger volume fraction of porosity, which can be attributed to improper fusional bonding between two successive hatches. At a given hatch spacing, the lack of fusion voids can be minimized by

FIGURE 9 Geometric relationships used in the simplified approach to estimate the probability of different positions in the part remaining unmelted.

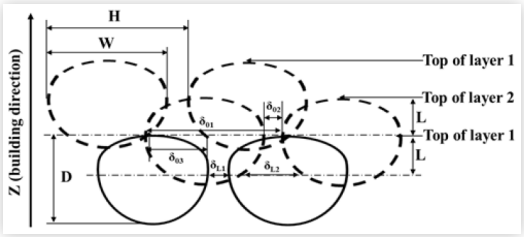

increasing the overlapping of the fused regions. This can be fulfilled by increasing the size of the molten pool at higher laser beam powers and/or lower scanning speeds as illustrated in Figure 10 (a) and (b), respectively. The relative density can reach 99.1% by increasing the power to 600 W (laser speed is 0.3 m/s) or lower the scanning the speed to 0.1 m/s (Power is 400 W). On the other hand, the peak porosity volume fraction became as high as 29.11% when the laser power is 350 W and the scanning speed is 0.3 m/s. Therefore, a low lack of fusion voids can be tuned by optimizing the process parameters [5].

3.1.3. Microstructure Reconstruction Via Dream.3D The porosity values were input into Dream. 3D to reconstruct the desired microstructures. Since porosity effect on mechanical behavior is the main concern of this study, the grain shape was considered as equiaxed in all the generated microstructures. Figure 11 shows the microstructures with 5% volume fraction porosity, where pores are in white color, and one representative was marked by a black dashed circle. Figure 12 shows the comparison of the shape and location of pores between experimental and regenerated results, both are in irregular shape that are a typical characteristic of the lack of fusion voids [20]. The microstructures were exported as Los Alamos FFT files, which acted as the input files into the EVP-FFT model for the investigation of the effect of porosity on mechanical properties.

FIGURE 10 The effect of (a) laser beam power (speed 0.3 m/s) and (b) laser beam speed (laser beam power 400 W) on the porosity level for the 3 layer and 3 hatch build with the layer thickness fixed as 0.3 mm.

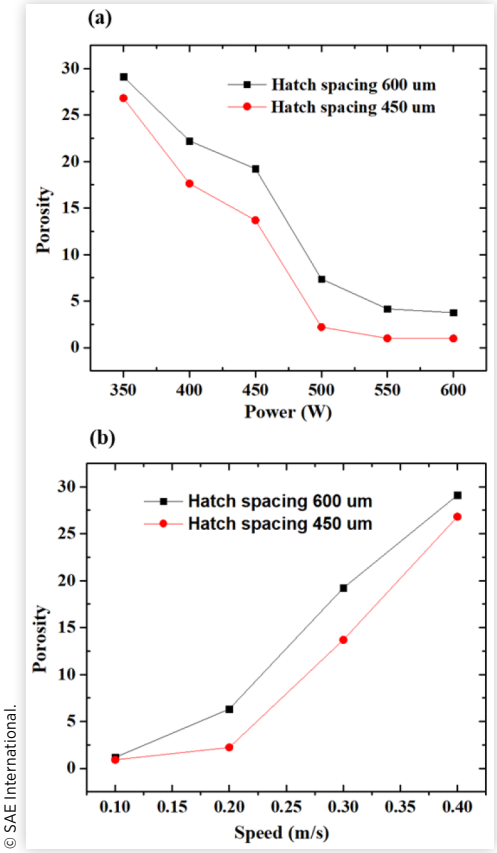

FIGURE 11 Microstructure generated by Dream. 3D with 5% porosity volume fraction. (b) is a cross section view of (a), where one representative pore with white color is marked by a black dashed circle.

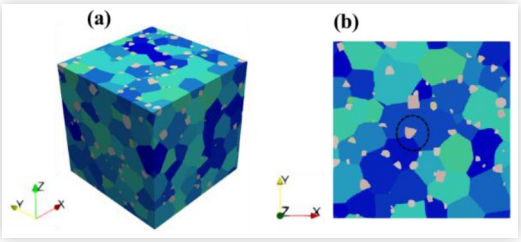

3.2. Structure-Property Relationship

3.2.1. Result of EVP-FFT Formulation To investigate the porosity effect on mechanical behaviors, the 3D cubic simulation domain was discretized into a 128 × 128 × 128 grids, and a periodic boundary condition was applied on the simulation domain. The uniaxial tension was implemented along z direction by applying a tensile strain of 3.5%, at a rate of 1.0 s^{-1}. The elastic constants and hardening parameters of AlSi10Mg adopted in this study are listed in Table 3 [20]. As depicted in Figure 13 the stress-strain curve obtained from simulation agreed well with the experiment [20].

Figure 14 shows the effect of porosity on the stress-strain relationship. A higher volume fraction of porosity has a lower

TABLE 3 Elastic constants and hardening parameters used in this study.

Elastic constant (GPa)	Hardening parameters (MPa)
C11 = 77.49	$\tau 0$ = 74.5
C12 = 27.12	$\tau 1$ = 224
C13 = 27.12	$\theta 0$ = 400
C44 = 25.19	$\theta 1$ = 250

FIGURE 12 Microstructure comparison between (a) a microstructure generated by Dream.3D and (b) a microstructure observed from scanning electron microscope [19], where the pores are marked by dashed black circles.

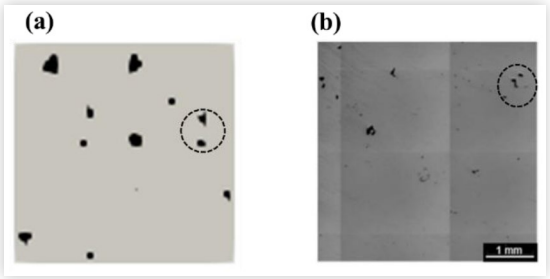

stress at the same strain. The result shows that the porosity has a significant effect on mechanical behavior. Figure 15 shows local stress and strain fields with 5% (a)(b) and 2% (c) (d) volume fraction of porosity, respectively. The inhomogeneous stress field was observed due to different orientations of grains. Zero stress and strain were obtained for the regions of pores as marked by a white circle, which may attribute their zero stiffness. Stress concentration can be noticed at the interface region between the grain and pores because of a strong mismatch between their elastic constants. This phenomenon will induce severe inhomogeneity and in turn make a negative contribution to overall stiffness of the material.

FIGURE 13 Stress-strain curve. (a) Model calibration and (b) porosity effect on stress-strain relationship.

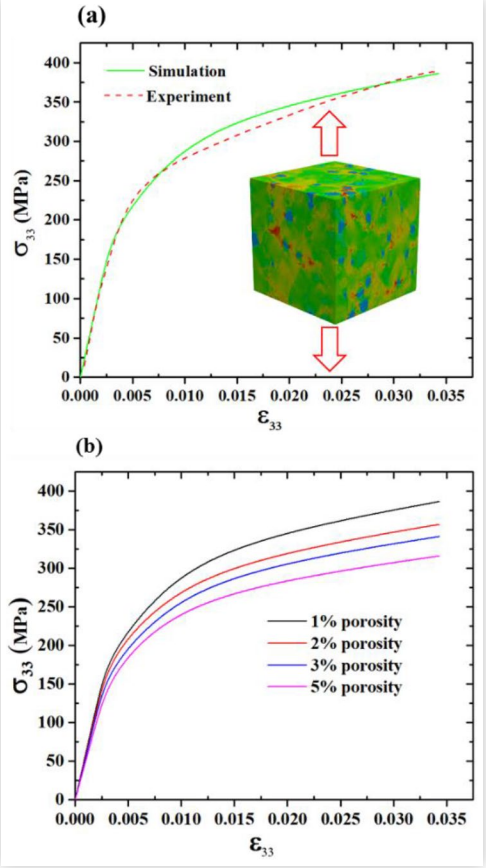

FIGURE 14 Strain and stress fields calculated by EVPFFT with 5% porosity volume fraction (a) (b) and 2% porosity volume fraction (c) (d), where blue color indicates null stress of pores.

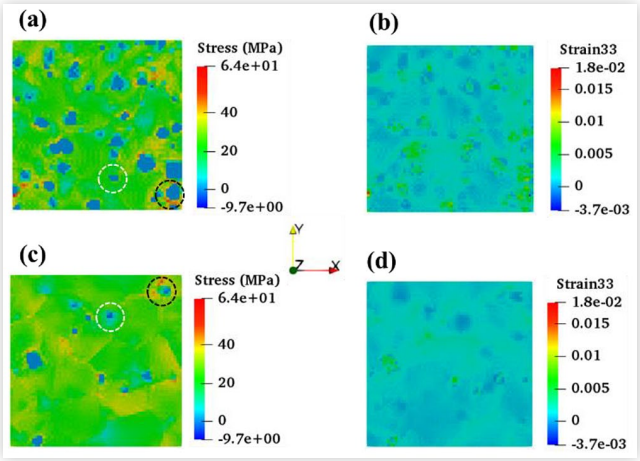

4. Conclusions

In summary, an integrated multi-scale multi-physics framework incorporated FE-based thermal model, Dream. 3D, and EVP-FFT micromechanical model has been developed and applied to the study of the process-structure-property relationship during metallic additive manufacturing. Following conclusions have been drawn from this study:

1. The process parameters have significant effects on the alloy's microstructure and properties. An appropriate combination of them including laser beam power, scanning speed, hatching spacing and layer thickness would greatly enhance the material performance. In this study, optimal process condition would be a laser power of 400 W at a scanning speed of 0.1 m/s, which would yield products with 99.1% relative density.
2. Porosity have significant effects on the material's mechanical behavior. Cracks and fatigue will be caused by high volume fractions of lack of fusion voids.
3. This established framework together with the approach of integrating phase field model to investigate the effect of thermal field on grain microstructures can be used to investigate more thoroughly the relationship among process, microstructure, and property.

Acknowledgements

This work is financially supported by NSF CMMI 1662854. The computer simulations were carried out on the clusters of High-Performance Computing Collaboratory (HPC^2) at Mississippi State University (MSU). The authors are thankful for the support provided by the Center for Advanced Vehicular Systems (CAVS) at MSU.

References

1. Uriondo, A., Esperon-Miguez, M., and Perinpanayagam, S., "The Present and Future of Additive Manufacturing in the Aerospace Sector: A Review of Important Aspects," *Proceedings of the Institution of Mechanical Engineers, Part G: Journal of Aerospace Engineering* 229(11):2132-2147, 2015.
2. Martin, J.H., Yahata, B.D., Hundley, J.M., Mayer, J.A. et al., "3D Printing of High-Strength Aluminium Alloys," *Nature* 549(7672):365-369, Sep 20, 2017, doi:10.1038/nature23894.

3. Perkins, R.A., Yang, W.-H., Liu, Y.-C., Chen, L., and Yenusah, C., "Finite Element Analysis of the Effect of Porosity on the Plasticity and Damage Behavior of mg AZ31 and Al 6061 T651 Alloys," in *IMECE2019-10672, Proceedings of ASME 2019 International Mechanical Engineering Congress & Exposition*, Salt Lake City, UT, November 11-14, 2019.
4. King, W.E. et al., "Observation of Keyhole-Mode Laser Melting in Laser Powder-Bed Fusion Additive Manufacturing," *Journal of Materials Processing Technology* 214(12):2915-2925, 2014, doi:10.1016/j.jmatprotec.2014.06.005.
5. Tang, M., Pistorius, P.C., and Beuth, J.L., "Prediction of Lack-of-Fusion Porosity for Powder Bed Fusion," *Additive Manufacturing* 14:39-48, 2017, doi:10.1016/j.addma.2016.12.001.
6. Wang, X., Liu, P.-W., Ji, Y.-Z., Liu, Y.-C. et al., "Investigation on Microsegratation of IN718 Alloy during Additive Manufacturing Via Integrated Phase-Field and Finite Element Modeling," *Journal of Materials Engineering and Performance* 28(2):657-665, 2019.
7. Liu, P.-W., Wang, Z., Xiao, Y.-H., Lebensohn, R.A. et al., "Integration of Phase-Field Model and Crystal Plasticity for the Prediction of Process-Structure-Property Relation of Additively Manufactured Metallic Mateirals," *International Journal of Plasticity* 128, 2020.
8. Liu, P., Cui, X., Deng, J., Li, S. et al., "Investigation of Thermal Responses during Metallic Additive Manufacturing Using a "tri-Prism" Finite Element Method," *International Journal of Thermal Sciences* 136:217-229, 2019, doi:10.1016/j.ijthermalsci.2018.10.022.
9. Yan, W. et al., "Multi-Physics Modeling of Single/Multiple-Track Defect Mechanisms in Electron Beam Selective Melting," *Acta Materialia* 134:324-333, 2017, doi:10.1016/j.actamat.2017.05.061.
10. Yan, W. et al., "Meso-Scale Modeling of Multiple-Layer Fabrication Process in Selective Electron Beam Melting: Inter-Layer/Track Voids Formation," *Materials & Design* 141:210-219, 2018, doi:10.1016/j.matdes.2017.12.031.
11. Tari, V. et al., "Validation of Micro-Mechanical FFT-Based Simulations Using High Energy Diffraction Microscopy on Ti-7Al," *Acta Materialia* 154:273-283, 2018, doi:10.1016/j.actamat.2018.05.036.
12. Kanjarla, A.K., Lebensohn, R.A., Balogh, L., and Tomé, C.N., "Study of Internal Lattice Strain Distributions in Stainless Steel Using a Full-Field Elasto-Viscoplastic Formulation Based on Fast Fourier Transforms," *Acta Materialia* 60(6-7):3094-3106, 2012, doi:10.1016/j.actamat.2012.02.014.
13. Liu, S., Zhu, H., Peng, G., Yin, J., and Zeng, X., "Microstructure Prediction of Selective Laser Melting AlSi10Mg Using Finite Element Analysis," *Materials & Design* 142:319-328, 2018, doi:10.1016/j.matdes.2018.01.022.
14. Yin, J. et al., "A Finite Element Model of Thermal Evolution in Laser Micro Sintering," *The International Journal of Advanced Manufacturing Technology* 83(9-12):1847-1859, 2015, doi:10.1007/s00170-015-7609-x.
15. Lebensohn, R.A., Kanjarla, A.K., and Eisenlohr, P., "An Elasto-Viscoplastic Formulation Based on Fast Fourier Transforms for the Prediction of Micromechanical Fields in Polycrystalline Materials," *International Journal of Plasticity* 32-33:59-69, 2012, doi:10.1016/j.ijplas.2011.12.005.
16. Michel, J.C. and Moulinec, H., "A Computational Method Based on Augmented Lagrangians and Fast Fourier Transforms for Composites with High Contrast," *CMES* 1(2):79-88, 2000.
17. Mukherjee, T., Wei, H.L., De, A., and DebRoy, T., "Heat and Fluid Flow in Additive Manufacturing - Part II: Powder Bed Fusion of Stainless Steel, and Titanium, Nickel and Aluminum Base Alloys," *Computational Materials Science* 150:369-380, 2018, doi:10.1016/j.commatsci.2018.04.027.
18. Li, Y. and Gu, D., "Parametric Analysis of Thermal Behavior during Selective Laser Melting Additive Manufacturing of Aluminum Alloy Powder," *Materials & Design* 63:856-867, 2014, doi:10.1016/j.matdes.2014.07.006.
19. DebRoy, T. et al., "Additive Manufacturing of Metallic Components - Process, Structure and Properties," *Progress in Materials Science* 92:112-224, 2018, doi:10.1016/j.pmatsci.2017.10.001.
20. Meng Zhang, C.-N.S., "Competing Influence of Porosity and Microstructure," in *Proceedings of the 28th Annual International Solid Freeform Fabrication Symposium*, 2017.

Contact Information

Dr. Yucheng Liu (SAE Fellow, ASME Fellow, PE), Department of Mechanical Engineering, Mississippi State University, Mississippi State, MS 39762-9552, USA; liu@me.msstate.edu**;** (662)325-1536

ISSN 0148-7191